Optimal frequency combs from cnoidal waves in Kerr microresonators

Dora Kholmyansky and Omri Gat
Racah Institute of Physics, The Hebrew University, Jerusalem 9190401, Israel

(Received 10 February 2019; revised manuscript received 27 August 2019; published 4 December 2019)

We present a thorough computational study of the existence, stability, and comb properties of cnoidal waves—dissipative periodic patterns—in Kerr microresonators. We show that cnoidal waves comprise a large set with multiple periods. Optimal comb power efficiency and bandwidth are obtained for highly red-detuned, intermediate-strength pump, and short-period waves, that are similar to a train of cavity solitons. We demonstrate a deterministic access path for optimal waves that yields combs of soliton-class bandwidth with a much higher power efficiency.

DOI: 10.1103/PhysRevA.100.063809

I. INTRODUCTION

Frequency comb generation from Kerr microresonators has seen rapid progress [1], recently achieving octave-spanning bandwidth through the emission of dispersive waves, facilitating carrier-envelope phase locking [2,3]. This breakthrough has been reached by driving the resonator to cavity-soliton steady states [4]. Solitons have the advantage of large bandwidth and a stable coherent spectrum, but are intrinsically hard to access because they exist only in regions of resonator parameter values where several stable steady waveforms coexist. Moreover, solitons only exist for a red-detuned pump, making them susceptible to thermal instabilities [5], while utilizing a small fraction of the pump power [6–8].

These difficulties necessitated the design of elaborate *ad hoc* control protocols for the pump parameters—power and frequency—to produce solitons in the resonator. However, cavity solitons suffer another basic drawback: Unlike laser solitons, cavity solitons form on top of a strong continuous-wave pedestal [9]; as a consequence the pump line carries a significant fraction of the total power, while the share of the comb power decreases as the ratio of cavity length and soliton width increases. The pedestal becomes weak for very large detuning, but then the output coupling becomes very inefficient [10].

In this view, it is imperative to search for stable frequency combs from other strongly nonuniform steady waveforms. Of these, the simplest are cnoidal waves (CnWs)—periodic solutions, also known as Turing rolls [8,11,12]. Stable periodic patterns are a universal feature of pattern-forming systems with a finite-wavelength instability [13], and as such appear in many nonlinear wave systems, including multimode lasers [14].

Unlike solitons, microresonator CnWs are directly accessible by raising the power of a blue- or moderately red-detuned pump beyond the modulational instability threshold, where the unstable continuous wave evolves directly into a low-amplitude CnW, sometimes called primary combs. For this reason they have been long recognized as precursors to the creation of full frequency combs [15]. However, as shown here, the manifold of stable CnWs extends far beyond the modulational instability threshold and contains waveforms with peak power and bandwidth on par with solitons, while enjoying comb power efficiency of 90% and higher. Moreover, for each choice of pump power and detuning there is a large family of stable CnWs with different periods, offering a large space for waveform optimization.

The next-simplest steady states are localized patterns, cavity solitons. Such patterns can arise as a kink-antikink connection between stable continuous waves and CnWs, or as an orbit homoclinic to the continuous-wave state [16,17]. In all cases solitons are multistable with continuous waves and therefore cannot be reached deterministically from continuous waves. Unlike CnWs, there are only two soliton solutions for any given pump parameters, of which at most one is stable.

More elaborate steady states can be constructed from multisolitons—kink-antikink connection with several oscillations, and bound-state combinations of these and single solitons. CnWs may be viewed as a special case of such patterns, in which the pulses are uniformly spaced, and have recently been studied experimentally under the name of perfect soliton crystals [18]. However, there is a crucial difference between CnW and nonperiodic arrays of pulses. Tail overlap induces interaction between the pulses in a many-soliton waveform, which gives rise to pulse drift in a random configuration of pulses, so that only specific configurations of interpulse spacings yield steady states, and the steady-state spacings are currently unknown. On the other hand, the periodicity of CnWs makes that the net interpulse interaction vanishes in the steady state and stabilizes the CnW against small perturbations, so that stable CnWs are obtained for continuously varying periods. Nevertheless, the interpulse interactions destabilize the CnWs at large separations, so that the CnW branch is not connected to the soliton branch except in the lossless case [12].

In spite of this strong motivation, so far there has been no comprehensive study of CnWs in microresonators, and even their domain of stability in parameter space has been only roughly mapped. The reason is that periodic solutions can be calculated analytically only for low-amplitude waves [17,19,20] and for lossless dynamics, equivalent to the limit of

high detuning [12], while study by simulation or experiments is resource-intensive.

We tackle this difficulty with the dynamical continuation method [8,16,20–22], which allows us to calculate numerically a large set of CnWs as a function of three parameters—pump amplitude, detuning, and wave period—and in this way to draw the stability boundary in a large region of parameter space. We then proceed to optimize the cavity waveform by using two benchmarks, comb power efficiency and rms bandwidth, defined precisely below.

We found that CnWs generated with both highly red-detuned and blue-detuned pumps can be optimal. The red-detuned combs are particularly interesting: They are quite similar to solitons, but have a higher repetition rate and, accordingly, a better power efficiency. Interestingly, the best performance in terms of comb power efficiency and bandwidth is obtained for intermediate pump power; increasing pump strength beyond the optimal point pushes power mostly into the pedestal, reducing the comb power efficiency and bandwidth (see top panel of Fig. 4).

While motivated by microcomb applications, our results are applicable to any driven Kerr resonator, including fiber resonators [23,24]. Moreover, the driven-damped nonlinear Schrödinger equation is a universal amplitude equation, so that it describes waves in a wide family of nonlinear resonators. The spatial version of the model was introduced in optics in Ref. [19], and other applications include driven condensates [25] and plasma waves [26].

II. STEADY CNOIDAL WAVES AND THEIR STABILITY

We model the resonator with the standard Lugiato-Lefever equation

$$\frac{\partial\psi}{\partial t} = -(1+i\alpha)\psi + \frac{i}{2}\frac{\partial^2\psi}{\partial x^2} + i|\psi|^2\psi + f, \tag{1}$$

where loss, anomalous dispersion, and Kerr are normalized by the appropriate choice of units for time t, resonator propagation length x, and resonator field envelope ψ; $f > 0$ and α are the pump amplitude and detuning, respectively. Normalization with typical experimental values [7,27,28] gives a time unit in the range of 10–100 ns, and a wave-number unit that corresponds to an output signal modulation frequency of a few THz to a few tens of THz. CnWs are steady nonuniform solutions $\psi(x)$ of Eq. (1) with a fundamental period p: $\psi(x+p) = \psi(x)$ for all x. Thus, the numerical task involved in calculating CnWs is the solution of the ordinary differential equation obtained from Eq. (1) upon setting the time derivative to zero. This is easily achieved near for f slightly above the continuous-wave modulational instability threshold $f_m(\alpha) = [1+(\alpha-1)^2]^{1/2}$ for $\alpha < \alpha_c = 41/30 \approx 1.37$, where a branch of the CnW bifurcates with low amplitude from the continuous wave. We call the stable part of this branch the principal branch of the CnW. Starting from the modulational instability threshold we used dynamical continuation methods [21,22] to map the part of the principal branch of the CnW for α between -4 and 6, and all f and p.

The analytical and numerical methods used to calculate the CnW and their stability are detailed in the Appendix. We show there that the great majority of CnWs are reflection-symmetric, and for given pump parameters they arise in one-parameter families parametrized by p. Because the CnWs bifurcate from continuous waves unstably for large α, we followed the red-detuned part of the principal branch by continuing from small to large α rather than by changing f, thus avoiding the need to follow unstable and secondary stable branches.

As detailed in the Appendix, the CnWs are susceptible to three types of instabilities distinguished by the wavelength of the fastest-growing perturbation. These are the long-wave type-E instability, type-H instability whose wavelength is $2p$, and type-F instability of wavelength p.

Figures 1 and 2 present constant-α two-dimensional sections of the three-parameter domain of stability of the principal branch of a CnW. For a given α, the principal branch occupies a finite region in the space of possible periods and pump amplitudes, bounded by instability curves. Each point in the interior of the section corresponds to a specific stable CnW solution of Eq. (1). In Fig. 1 the stability zones are colored by the comb power efficiency

$$\eta_c = \frac{P_c}{P_t}, \tag{2}$$

where

$$P_c = \int \frac{dx}{L}|\psi(x)|^2 - \left|\int (dx/L)\psi(x)\right|^2, \tag{3}$$

$$P_t = \int \frac{dx}{L}|\psi(x)|^2, \tag{4}$$

are, respectively, the comb power and the total power; the same sections are colored in Fig. 2 by the rms bandwidth,

$$\Omega_b = \sqrt{\frac{1}{P_t}\int \frac{dx}{L}|\psi'(x)|^2}. \tag{5}$$

For $\alpha > \alpha_c$ there is an overlap between the CnW and continuous-wave stability regions. In the sections of Figs. 1 and 2 with such detunings, a gray dashed curve marks the upper boundary of the stability overlap.

The dependence of the CnW benchmarks on parameters and their optimization is discussed in the rest of the paper. We now summarize the main conclusions that can be drawn from Fig. 1 about the shape of the domain of stability of CnWs, the instability mechanisms, and its relation to continuous waves:

(1) The shapes of the stability domain sections are complex and generally become more so for increasing α. This complexity is caused by the participation of several instability modes. This is clearest in the $\alpha = -2.3$ section, where the two smooth parts boundary are associated with different instability mechanisms. For larger α the number of smooth parts the stability section boundary increases, up to eight for $\alpha = 5.88$, and we conjecture that each of these represents a different instability mode.

(2) When $\alpha < \alpha_c$ there is no overlap between the principal-branch CnW and the stable continuous wave, so that $f_m(\alpha)$, the upper stability boundary of the continuous wave, is also the lower boundary of the CnW stability. For these values of α, the CnW stability section has the cup-like shape that is typical for finite-wavelength, zero-frequency pattern-

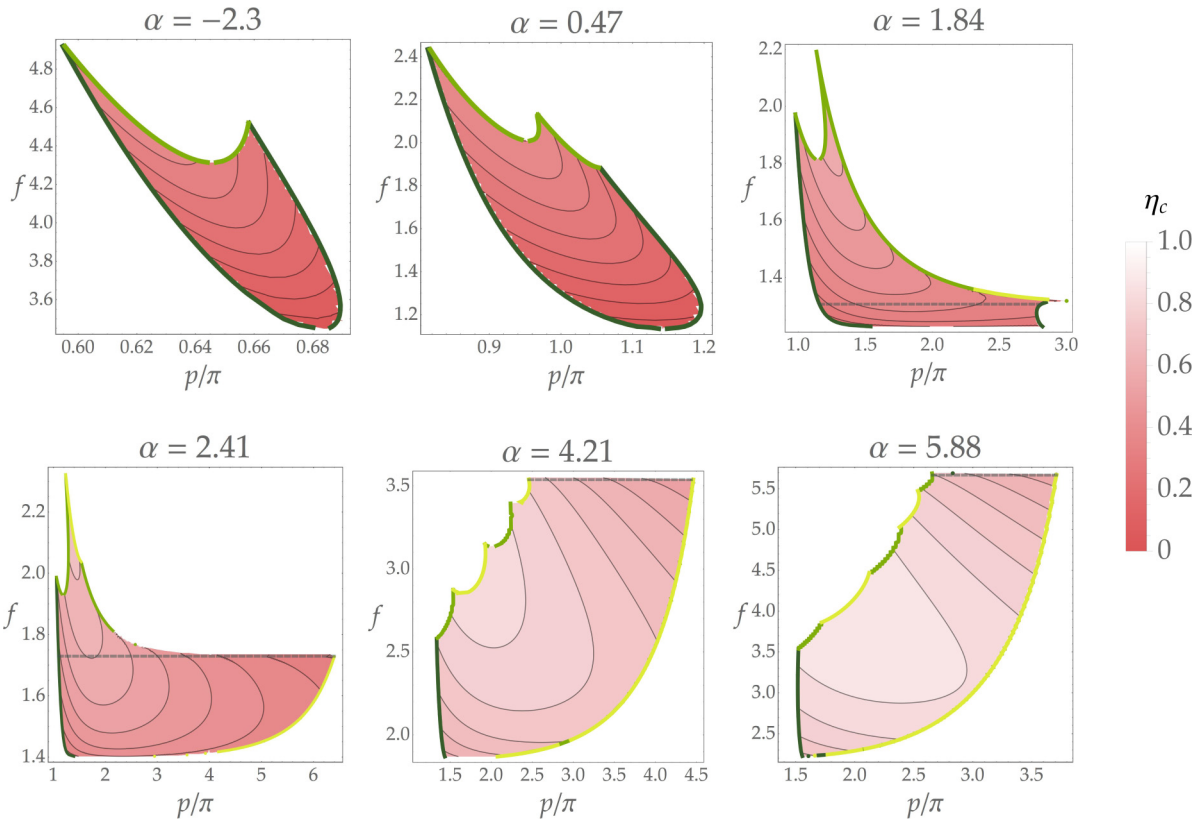

FIG. 1. Constant-α sections of the CnW stability domain in the α-f-p parameter space. The section boundaries are shown in thick (green) curves. The dark-, medium-, and light-hued parts of the boundary curves correspond to type-E, H, and F instabilities (respectively). Unstable CnWs may exist outside the section boundaries. Dashed horizontal lines, where present, are the upper stability limits of continuous waves. In other sections the upper limit of continuous-wave stability is at the bottom of the CnW stability region. The interiors of the sections are colored by the comb power efficiency η_c, according to the color key shown on the right.

forming systems, with CnWs susceptible to Eckhaus (type-E) instabilities in the neighborhood of the threshold.

(3) When $\alpha > \alpha_c$ there is a region of overlap between the principal branch and stable continuous waves. As shown below, CnWs in the overlap region are similar to a periodic trains of solitons. However, while the range of stable periods increases significantly at first, reaching more than 6π for $\alpha = 2.41$, it narrows back when α is further increased; this observation implies that the CnW and solitons belong to different branches. Interestingly, while for $\alpha = 4.21$ and $\alpha = 5.88$ the CnW stability sections are bounded above by the continuous-wave stability boundary (shown as a gray dashed line in the figures), for moderate values of α (e.g., $\alpha = 2.41$), there are nonsoliton-like stable CnWs for pump amplitudes beyond f_m.

III. OPTIMAL CNOIDAL WAVES

We now turn to the optimization problem. The colored regions in Fig. 3 correspond to pump parameters for which there is a principal branch CnW of *any* period—that is, they are the projection of the three-dimensional CnW stability domain on the α-f plane. The solid lines are the boundaries of this projection. The part of the lower boundary with $\alpha < \alpha_c$ (drawn in a lighter hue) is also the upper continuous-wave stability boundary. For $\alpha > \alpha_c$ the upper continuous-wave stability boundary is shown with a dashed line. Continuous waves are the only stable stationary waves in the pump-parameter region below the lower CnW stability boundary, while no stable stationary waves are known to exist in the region above the upper CnW and continuous-wave stability boundaries.

Each point in the CnW existence region shown in Fig. 3 is colored according to the maximal comb power efficiency η_c (top) and rms bandwidth Ω_b (bottom) among CnW of all stable periods p for the given pump parameters α and f. The results imply that power efficiency is mostly an increasing function of both α and f, but for highly red-detuned CnW, with $\alpha \gtrsim 4$ the maximal η_c is reached for f values in the interior of the stability domain. For such α the CnWs are similar to a train of solitons, and above the optimal f more power goes into the pedestals than into the solitons themselves, thereby reducing the comb power efficiency (see top panel of Fig. 4). The same principle implies that, for highly red-detuned CnWs, power efficiency is optimized for short periods (see Fig. 1, bottom right), which minimizes the length of the pedestal. The upshot is that the highest comb power efficiency in our calculations was obtained for large red detuning, intermediate pump strength, and short period, reaching 90% for $\alpha = 6.01$, $f = 4.07$, $p = 1.87\pi$; it is shown as a red dot in Fig. 3 (top).

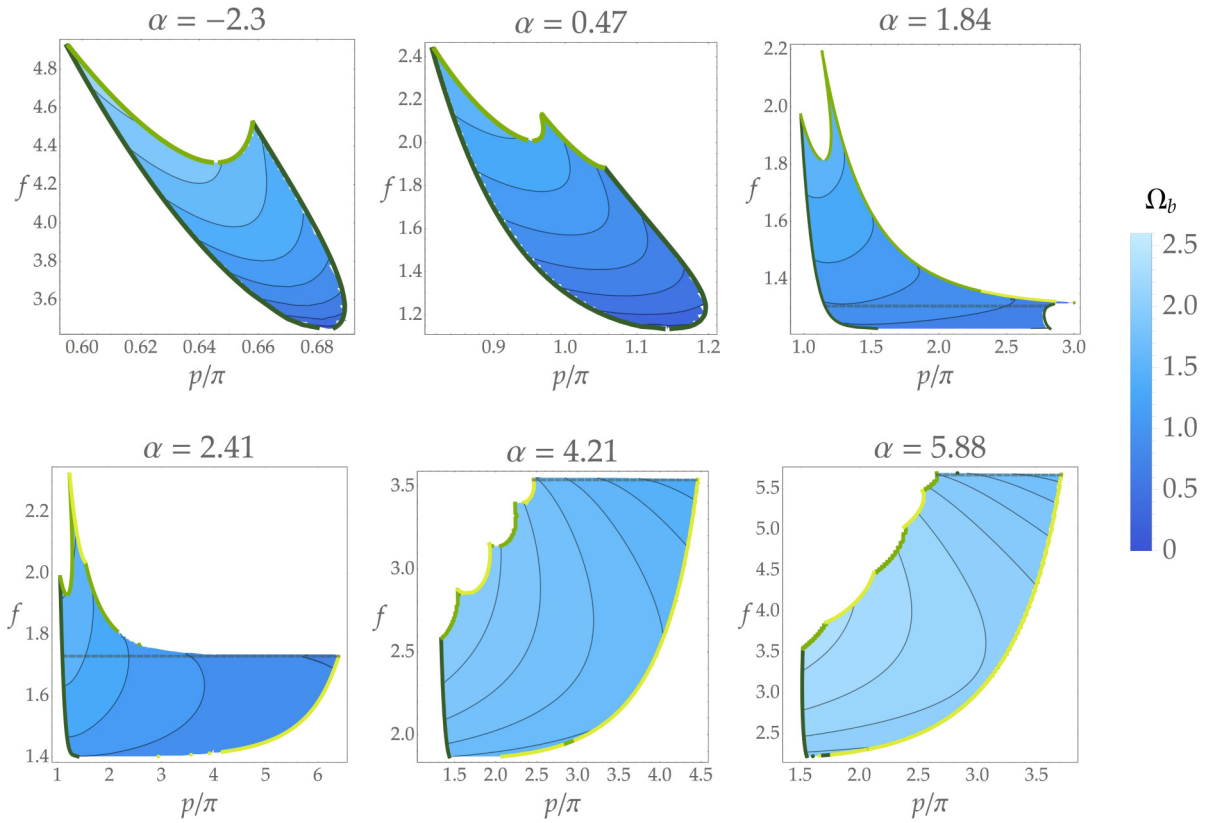

FIG. 2. Stability sections of Fig. 1, with interiors colored by the rms bandwidth Ω_b, according to the color key shown on the right.

Unlike comb power, the bandwidth becomes large in *both* highly blue- and red-detuned CnWs. In the latter case, optimal bandwidths are obtained for intermediate f and small p, for the same reason these are good conditions for power optimization; the η_c-optimal CnW exhibits $\Omega_b \approx 2.4$; but in the set of CnW studied here, the largest bandwidth is obtained for blue-detuned and strong pumps, reaching $\Omega_b = 2.6$ for $\alpha = -4$, $f = 6.79$, $p = 0.52$, shown as a blue dot in Fig. 3 (bottom). Although the blue- and red-detuned combs have comparable rms bandwidth, the $\alpha < 0$ comb shape is less favorable, since the intensity of the comb lines falls off faster in the tails than that of the $\alpha > 0$ comb tails. Moreover, blue-detuned combs are more widely spaced and require stronger pumps than comparable bandwidth red-detuned combs; the main advantage of blue-detuned CnWs is that they are easier to access than the red-detuned ones, as explained below in Sec. V.

Since the maximum power efficiency and bandwidth have been obtained on the boundaries of the detuning range considered here, it is clear that even higher values are reachable for larger detunings. In experimental applications, there is always a finite range of pump parameters, and ultimately the optimal combs have to be determined on a case-by-case basis. Still, we can draw the following broad conclusions from the present results.

Since the comb envelopes of CnWs in the highly red-detuned region are very close to those of solitons (see Sec. IV below), we can use known soliton properties [9,29], to predict that, as α increases, the pedestal decreases and the bandwidth increases. A smaller pedestal implies better comb power efficiency, but because the comb power efficiency of 90% is already achieved for $\alpha = 6$, the expected gains in power efficiency are small, and likely outweighed by decreasing conversion efficiency.

Bandwidth, on the other hand, can be significantly increased if a larger detuning range is available, where scaling arguments [29] imply that bandwidth grows asymptotically as the square root of the absolute detuning. For such combs, however, output coupling becomes a major consideration.

IV. CNOIDAL WAVES AND SOLITONS

Solitons and soliton bunches are waves that oscillate in some interval of the cavity and approach uniform continuous waves in the rest. Thus, these waves are found in the parameter regions of cw-CnW stability overlap [16,30], whose projection on the α-f plane is the region of the CnW stability domain in Fig. 3 below the dashed line (above $\alpha \approx 5$ the upper continuous-wave stability boundary is not distinguishable from that of CnW).

It is tempting therefore to think of solitons as a limiting case of large-period CnWs; however, the numerical results show that the range of stable CnW periods is always bounded from above, which means that it is not possible to access solitons by a smooth change of parameters starting from a principal-branch CnW. This conclusion agrees with the analysis of Refs. [17,30], which shows that solitons and soliton bunches belong to individual stable branches, which are not stably connected to the continuous waves. On the other hand, since the optimal red-detuned CnWs are very close in shape

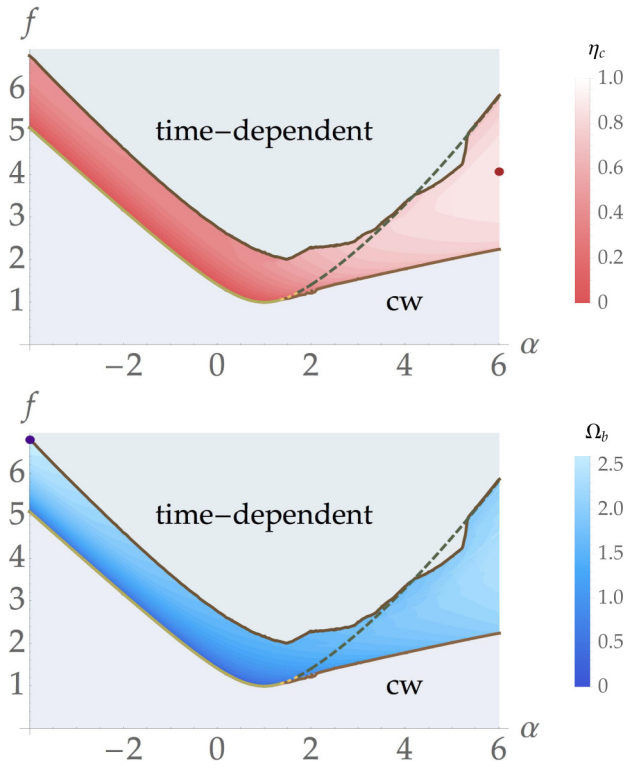

FIG. 3. Projection of the principal-branch CnW stability region on the α-f pump-parameter plane, colored by optimal comb power efficiency η_c (top) and rms bandwidth Ω_b (bottom). The light-hued part of the lower CnW stability boundary is at the same time the upper stability boundary of continuous waves for $\alpha < \alpha_c$. For $\alpha > \alpha_c$, the upper continuous-wave stability boundary is shown by the dashed line, of which the compatible part (see text) is colored in gold (light hue).

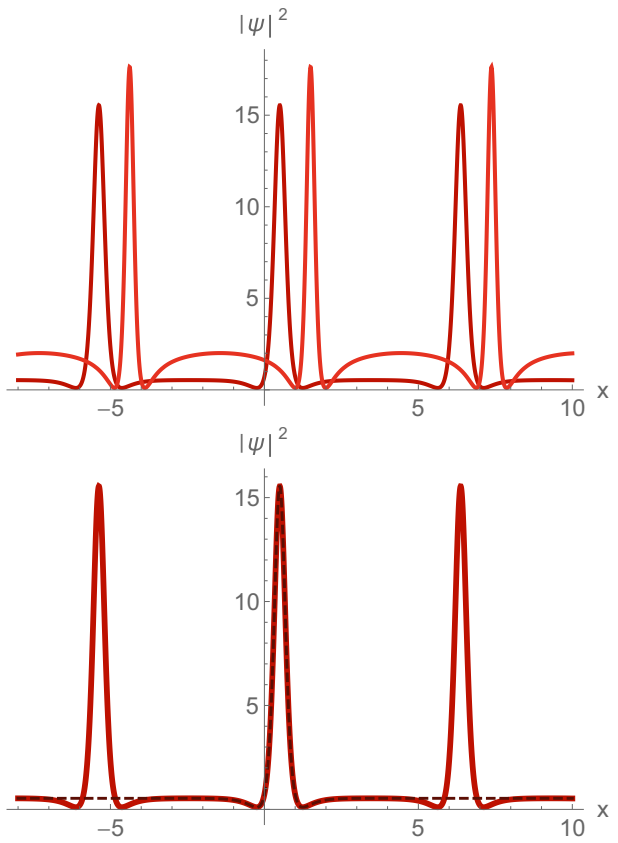

FIG. 4. (top) Intensity $|\psi|^2$ as a function of propagation length x of the CnW with period $p = 1.87\pi$ and pump parameters $\alpha = 6.01$, $f = 4.07$ (dark red) and of the $p = 2.35\pi$-period CnW for $\alpha = 6.01$, $f = 5.88$ (light red). (bottom) Same as for top panel but for $p = 1.87\pi$-period CnW (full dark red) and soliton (dashed black), with pump parameters $\alpha = 6.01$, $f = 4.07$.

to a train of solitons (see Fig. 4, bottom panel), CnW combs have the same bandwidth and envelope as soliton combs, and are largely accessible, as we show next.

V. ACCESSING CNOIDAL WAVES

The CnWs studied here belong to a single continuous branch of stable stationary solutions of Eq. (1). However, resonators impose periodic boundary conditions $\psi(x,t) = \psi(x+L,t)$, where the cavity length L is typically a few tens to hundreds of normalized length units in existing experimental systems [7,27,28]. Only a discrete set of periods, $p_n = L/n$, n integer, is compatible with these boundary conditions. The three-dimensional CnW stability domain is therefore sliced into several $p = p_n$ two-dimensional sections; a number of such sections are shown in Fig. 1 of Ref. [8].

Among the CnWs studied here, every solution in an L-compatible slice of the principal branch is also a stable CnW with L-periodic boundary conditions. The converse is not strictly true, however, since instability modes need not satisfy the periodic boundary conditions. Consequently, the n-period CnW finite-L stability region may be somewhat larger than the corresponding slice of the principal branch; still, since in practice L values are large, the finite-length effects are likely to be quite small. Indeed, the union of the α-f projection of the p_n stability sections in Ref. [8] is well approximated by the principal branch projection shown in Fig. 3 of this paper.

Since for any fixed L, the CnW principal branch is sliced into disjoint parts, two stable CnWs can be continuously joined only if they have the same period. A common method to access CnWs has been to start from α, f values where only the continuous waves are stable, and cross the modulational instability curve $f_m(\alpha) = [1 + (\alpha - 1)^2]^{1/2}$ at a point where $\alpha < \alpha_c$, so the instability is supercritical [31]. A low-amplitude CnW then forms as a result of the instability, with a period p that is the closest to that of the least-stable mode, $p_m(\alpha) = \sqrt{2/(2-\alpha)}\pi$.

At this point, the period p is locked in the sense that any adiabatic change in the pump leads to a continuous evolution of the CnW in the principal branch with the same period, as long as there exists a stable CnW for these parameters. If the pump power is further increased with fixed detuning, however, this protocol quickly runs into further instabilities, before a broad frequency comb can develop, because the fixed α stability domain tilts to lower α in the supercritical regime (see first two panels of Figs. 1 and 2). Much better combs can be reached if α and f are increased *together*, for example, along a diagonal in the parameter plane. In this way, all L-compatible CnWs with $p < p_m(\alpha_c) \approx 1.78\pi$ can

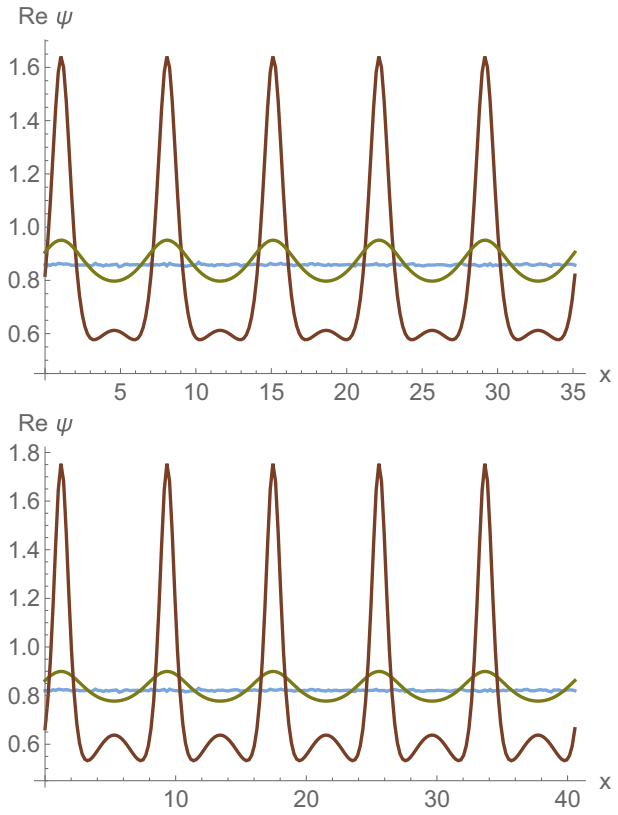

FIG. 5. The real part of the waveform obtained by numerical simulation of Eq. (1) with pump parameters $\alpha = 1.6$ (top) and $\alpha = 1.7$ (bottom) in the threshold-compatible interval, and $f = f_m(\alpha) + 10^{-4}$, slightly above the modulational instability threshold, in a cavity length of $5p_m(\alpha)$, where p_m is the period of the critical mode. Initial conditions (light blue) are randomly perturbed continuous waves. In both cases, like for others not shown here, the critical mode initially grows harmonically (medium green), before settling on the period-p_m principal branch CnW (dark brown).

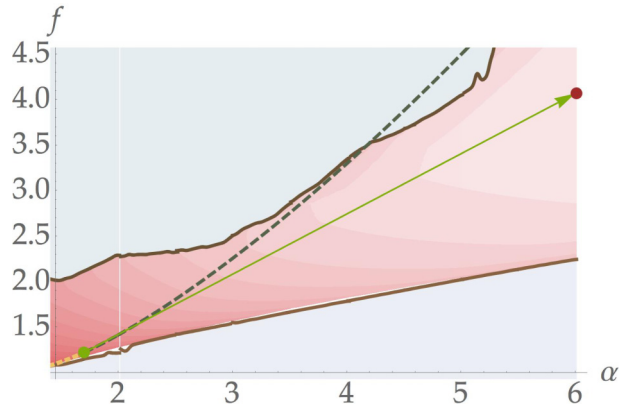

FIG. 6. A deterministic access path in pump-parameter space starting with compatible subcritical modulational instability (green dot) and following the green arrow to the comb power efficiency optimal CnW (marked with a red dot). If pump detuning α and amplitude f can only be controlled separately, the diagonal path should be replaced by a step-shaped path (not shown) where f is first increased to 2.2, then α is increased from 1.7 to 6, and then f is increased again to its final value of 4.07.

be deterministically accessed. Such an access path can reach the blue-detuned optimal CnW of Fig. 3 and get close to the red-detuned optimal waveform.

The supercritical access method is limited in the range of possible periods because the long-period instabilities are subcritical, which means that there are no small-amplitude CnWs near the instability threshold. This limits access to the optimal red-detuned waves, whose period is larger than 2π. Nevertheless, we now show that a slight variation of the access method just presented significantly extends the range of obtainable periods.

Toward this goal we note first that, when the modulational instability curve is crossed with $\alpha_c < \alpha < 2$, small fluctuations in the continuous wave starts growing, and the fastest growing mode is the one with period p_g closest to $p_m(\alpha)$, just as in the supercritical instability. What happens next depends on the extent of the principal branch near the bifurcation point α, $f_m(\alpha)$. Since this is a subcritical instability, the principal branch includes a range of periods of stable CnWs for these pump parameters; this range is shown as a horizontal dashed line in the last four panels of Figs. 1 and 2. If this range contains the period p_g, then the initial perturbation grows fast initially, eventually saturating at the corresponding large-amplitude CnW, as shown in Fig. 5. In this case we say that the instability is *threshold compatible* with the principal branch; our principal-branch calculations show that the instability is threshold compatible when $\alpha < \alpha_t \approx 1.71$ (shown as the gold-colored part of the continuous-wave stability boundary in Fig. 3). Higher detuning values are threshold incompatible, and for these values of α the modulational instability leads to CnWs with periods smaller than p_g, or to nonperiodic waveforms.

Thus, crossing the threshold-compatible subcritical part the instability curve, leads to the formation of a finite-amplitude CnW with periods up to $p_m(\alpha_t) \approx 2.62\pi$. This CnW may then serve as a starting point for a diagonal access path in pump-parameter space, which can reach essentially all of the highly-red-detuned CnWs shown in Fig. 3, including the optimal one. An example of a pump-parameter access path leading to the comb power efficiency optimal CnW is shown in Fig. 6, and snapshots from the evolution of the waveform along this path, starting from the steady state shown in the bottom panel of Fig. 5 (brown curve) are shown in Fig. 7.

VI. CONCLUSIONS

Cnoidal waves in microresonators are useful for two purposes: as comb sources themselves, and as an intermediate step toward other types of waveforms, including solitons. A distinguishing feature is the coexistence of a *family* of CnWs for each pump-parameter choice, with continuously varying periods. It becomes a large discrete family when the boundary conditions of a specific cavity are imposed, most of which is accessible directly and deterministically from the continuous wave by following a path in pump-parameter space where pump detuning and power are simultaneously or consecutively increased. The access path can be followed either by simultaneous control of the pump strength of detuning, or by a

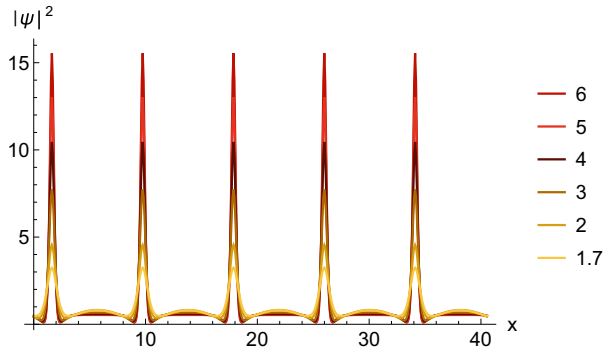

FIG. 7. Snapshots showing the growth of a CnW along the access path of Fig. 6. Legend shows the detuning values α of the CnW.

step-like approximation of it in applications where the pump parameters can only be controlled individually.

Using comb power efficiency and bandwidth as benchmarks, it turns out that the optimal CnW combs are produced for highly-red-detuned and intermediate-strength pumps. Our numerical results were obtained for a finite interval of detunings, and we find that both the highest comb power efficiency and bandwidth are obtained on the boundaries of this interval, so that these are not globally optimal values. Since experiments have access to a finite range of detunings, experimental CnWs would be optimized on the boundary as well. Bandwidth especially can be further improved, but this improvement comes at the expense of lower output comb power, because the output coupling becomes inefficient for very large detunings.

The optimal red-detuned CnWs coexist with solitons, and both waveforms have the same comb envelope and, in particular, the same bandwidth. Unlike solitons, CnWs can be accessed deterministically, and they produce stronger comb lines, which are more widely spaced. Moreover, in the parameter range studied here, the red-detuned CnW combs utilize the cavity power much more efficiently than solitons, where a significant fraction of the power is carried by the continuous-wave pedestal. Allowing for larger detunings mitigates this problem for solitons at the price of low conversion efficiency. Since the output coupling for solitons and red-detuned CnWs is expected to be similar, we predict that the *output* power efficiency is optimal for moderately-red-detuned CnWs of the type studied here, although further study is necessary to settle this point.

At present, soliton microcomb applications rely on dispersive wave broadening. The similarity of CnWs to soliton comb shapes makes it likely that the mechanism is applicable to CnWs as well. Although the question of thermal resilience was not addressed here, given that thermal instabilities generally affect red-detuned waves [1], optimal blue-detuned CnWs are likely to be thermally stable.

Compared with solitons, CnW combs are characterized by high repetition rate, which in current experimental systems would be at least a few hundreds of GHz. This issue may be solved with the dual comb technique, recently demonstrated in Ref. [32]. A better solution would replace the CnW by a nonperiodic train of solitons or a soliton crystal by introducing defects [28], retaining the good CnW comb properties, with a free spectral range repetition rate. A systematic study of soliton crystals, their stability and access path is beyond the present scope.

ACKNOWLEDGMENTS

We have benefited from illuminating discussions with Curtis R. Menyuk and Zhen Qi and thank them for sharing preliminary results with us and for critical remarks. We thank Aurelien Coillet for helpful remarks and Ergun Simsek for careful reading of the paper while in preparation. This work was supported by the Israel Science Foundation.

APPENDIX: CNOIDAL WAVES, THEIR STABILITY, AND DYNAMIC CONTINUATION

In this Appendix we deduce general properties of periodic stationary solutions of Eq. (1). It follows from the translational symmetry of Eq. (1) that each CnW belongs to a one-parameter family of solutions $\psi(x-x_0)$, related to each other by a constant translation. The equation also has parity symmetry, from which it follows that there are two symmetry classes CnW. Reflection-symmetric solutions have an infinite set of symmetry points x_n, such that $\psi(x-x_n)=\psi(-x-x_n)$, separated by half-integer multiples of the period p. Non-reflection-symmetric CnWs have no symmetry points; reflection symmetry then implies that if $\psi(x)$ is a non-reflection-symmetric CnW, then $\psi(-x)$ is another CnW.

Calculating periodic solutions of a differential equation is a boundary-value problem, while general existence and uniqueness results are in general given for initial-value problems. For this reason it is necessary to determine the number of constraints that the solutions must obey.

It turns out that the answer to this question is different for the two reflection-symmetry classes. In the non-reflection-symmetric class, the solution of the initial-value problem is determined by four real parameters, $a_1,\ldots,a_4$, the real and imaginary parts (say) of ψ and its derivative at the initial point 0,

$$\psi(0)=a_1+ia_2,\quad \psi'(0)=a_3+ia_4. \tag{A1}$$

If we are looking for a CnW with period p, then the solution must obey the boundary conditions $\psi(p)=\psi(0)$ and $\psi'(p)=\psi'(0)$, which amount to four real (nonlinear) equations

$$z_k=a_k,\quad k=1,\ldots,4, \tag{A2}$$

where

$$\psi(p)=z_1+iz_2,\quad \psi'(p)=z_3+iz_4, \tag{A3}$$

and each z_k is a functions of a_k, that have to be solved for the a_k.

Let J be the matrix with elements

$$J_{kl}=\delta_{kl}-\frac{\partial z_k}{\partial a_l}. \tag{A4}$$

The inverse-function theorem implies that, if $\det J\neq 0$, then solutions of the system (A2) are isolated. However, translation symmetry implies that solutions actually belong to a one-parameter, so that J is rank three at most points. It follows

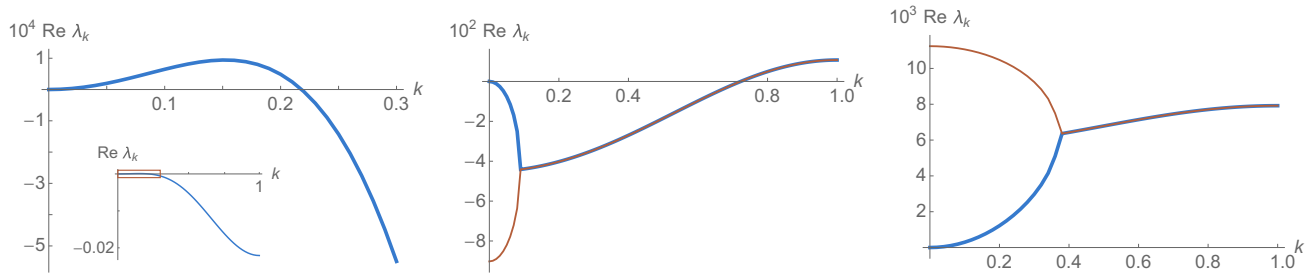

FIG. 8. Fundamental domain of stability spectra near instabilities of type E (left, detail, inset showing full domain, $\alpha = 1.84$, $f = 1.375$, $p = 1.14\pi$), H (middle, $\alpha = 1.84$, $f = 1.375$, $p = 2.92\pi$), and F (right, $\alpha = 1.84$, $f = 1.6$, $p = 1.54\pi$). Shown are the real parts of the hydrodynamic band (thick blue) and the least stable nonhydrodynamic band (amber, for the type-H and -F cases) as a function of stability wave number k in units of π/p, p being the CnW period. The two curves join for k values where the two least stable eigenvalues are a complex-conjugate pair. See text for further explanation.

that Eq. (A2) is overdetermined, and an additional parameter must be tuned to solve it. For fixed pump parameters this tuning parameter can only be the period p; it follows that non-reflection-symmetric CnWs arise only for a discrete set of periods.

Consider next reflection-symmetric CnWs. In this case, the boundary conditions are most naturally imposed at the symmetry points, where reflection symmetry implies that the derivative of ψ vanishes. The initial-value problem is therefore now defined by only two real parameters, b_1, b_2,

$$\psi(0) = b_1 + ib_2, \quad \psi'(0) = 0, \tag{A5}$$

where 0 has been chosen as one of the symmetry points without loss of generality. Periodicity implies that $p/2$ is a symmetry point neighboring 0. A period-p reflection-symmetric CnW must therefore obey the boundary conditions

$$y_1 = 0, \quad y_2 = 0, \tag{A6}$$

where the real-valued y_1 and y_2, defined by

$$\psi'(p/2) = y_1 + iy_2, \tag{A7}$$

are functions of the initial values b_1 and b_2.

Reflection-symmetric CnWs are thus obtained from the solution of the two-variable system (A6). Unlike the nonsymmetric CnW, solutions of (A6) do not belong to one-parameter families, because the boundary condition is obeyed only at the symmetry points. The matrix K with elements

$$K_{kl} = \frac{\partial y_k}{\partial b_l} \tag{A8}$$

is therefore full rank at most points, and by the implicit function theorem (A6) can be solved for CnWs depending smoothly on p. That is, in contrast with non-reflection-symmetric CnWs, reflection-symmetric CnWs arise in bands of variable periods for given pump parameters. For this reason reflection-symmetric CnWs are much more common than non-reflection-symmetric ones; the principal branch, in particular, consists of reflection-symmetric CnWs.

When the oscillation amplitude is small, weakly nonlinear solutions can be found through multiscale perturbation methods [17,19,20], but in general the waves have to be calculated numerically. The results presented here are based on a finite-difference discretization of the stationary Lugiato-Lefever equation, which yields a set of coupled algebraic equations. Together with the discretized boundary conditions, these equations form a well-posed problem for generic values of the parameters α, f, and p, which was solved here by damped Newton iterations [21].

The stability of a CnW $\psi_0(x)$ is studied, as always, by the linear dynamics of an infinitesimal perturbation $\psi_1(x,t)$; treating ψ_1 and its complex conjugate $\bar{\psi}_1$ as independent gives the linear system

$$\frac{\partial}{\partial t}\begin{pmatrix}\psi_1\\ \bar{\psi}_1\end{pmatrix} = L\begin{pmatrix}\psi_1\\ \bar{\psi}_1\end{pmatrix}, \quad L = \begin{pmatrix}-(1+i\alpha) + \frac{i}{2}\frac{\partial^2}{\partial x^2} + 2i|\psi_0|^2 & i\psi_0^2\\ -i\bar{\psi}_0^2 & -(1-i\alpha) - \frac{i}{2}\frac{\partial^2}{\partial x^2} - 2i|\psi_0|^2\end{pmatrix}. \tag{A9}$$

The periodicity of ψ_0 implies by Bloch's theorem [33] that the eigenvectors of L are quasiperiodic:

$$\begin{pmatrix}\psi_1(x)\\ \bar{\psi}_1(x)\end{pmatrix} = \begin{pmatrix}u(x)\\ v(x)\end{pmatrix}e^{ikx}, \tag{A10}$$

where u and v are p periodic, and k is defined up to an integer multiple of $2\pi/p$.

This means that, just like in quantum mechanics with a periodic potential, eigenvalues belong to continuous bands $\lambda_n(k)$, $|k| < \pi/p$, where n is a discrete index. Discrete symmetries simplify the numerical problem, so that each branch has to be calculated only for $k \geqslant 0$, and each eigenfunction has to be calculated only in the fundamental domain $0 \leqslant x \leqslant p/2$.

As in any system with spontaneously broken translational symmetry, the stability spectrum contains a $k = 0$ zero mode, which belongs to an eigenvalue band $\lambda_h(k)$ whose small k (large wavelength) part consists of soft hydrodynamic modes [34]. We call this band the hydrodynamic band.

The CnW ψ_0 is stable if all of the eigenvalues have a negative real part, other than the translational zero mode. We determined the stability by discretizing L using finite differences and calculating the least stable eigenvalue (that is, the one with largest real part) of the resulting matrix for a set k, thus obtaining the least-stable eigenvalue band.

For stable solutions, the hydrodynamic band must be the least-stable band with a zero maximum of $\mathrm{Re}\,\lambda_h$ at $k = 0$. We found that there are three mechanisms for loss of stability:

Type E: The hydrodynamic band remains least stable, but the extremum of $\mathrm{Re}\,\lambda_h$ at $k = 0$ becomes a minimum. It is an Eckhaus-type instability of large-wavelength perturbations [20].

Type H: The hydrodynamic band remains least stable with a maximum at $k = 0$, but another maximum of $\mathrm{Re}\,\lambda_h$ at $k = 1$ becomes positive. It is a harmonic instability where the period of the perturbation is $2p$. This perturbation mode conserves the total waveform power.

Type F: A nonhydrodynamic band λ_1 surpasses λ_h to become least stable, and $\mathrm{Re}\,\lambda_1$ has a positive maximum at $k = 0$. This is a non-power-conserving fundamental instability of period p.

Typical stability spectra for the three cases are shown in Fig. 8.

[1] T. J. Kippenberg, A. L. Gaeta, M. Lipson, and M. L. Gorodetsky, Science **361**, eaan8083 (2018).

[2] V. Brasch, M. Geiselmann, T. Herr, G. Lihachev, M. H. P. Pfeiffer, M. L. Gorodetsky, and T. J. Kippenberg, Science **351**, 357 (2016).

[3] M. H. P. Pfeiffer, C. Herkommer, J. Liu, H. Guo, M. Karpov, E. Lucas, M. Zervas, and T. J. Kippenberg, Optica **4**, 684 (2017).

[4] T. Herr, V. Brasch, J. D. Jost, C. Y. Wang, N. M. Kondratiev, M. L. Gorodetsky, and T. J. Kippenberg, Nat. Photonics **8**, 145 (2013).

[5] H. Guo, M. Karpov, E. Lucas, A. Kordts, M. H. P. Pfeiffer, V. Brasch, G. Lihachev, V. E. Lobanov, M. L. Gorodetsky, and T. J. Kippenberg, Nat. Phys. **13**, 94 (2016).

[6] X. Yi, Q.-F. Yang, K. Y. Yang, M.-G. Suh, and K. Vahala, Optica **2**, 1078 (2015).

[7] J. A. Jaramillo-Villegas, X. Xue, P.-H. Wang, D. E. Leaird, and A. M. Weiner, Opt. Express **23**, 9618 (2015).

[8] Z. Qi, S. Wang, J. Jaramillo-Villegas, M. Qi, A. M. Weiner, G. D'Aguanno, T. F. Carruthers, and C. R. Menyuk, Optica **6**, 1220 (2019).

[9] I. V. Barashenkov and Y. S. Smirnov, Phys. Rev. E **54**, 5707 (1996).

[10] C. Bao, L. Zhang, A. Matsko, Y. Yan, Z. Zhao, G. Xie, A. M. Agarwal, L. C. Kimerling, J. Michel, L. Maleki *et al.*, Opt. Lett. **39**, 6126 (2014).

[11] A. Coillet, I. Balakireva, R. Henriet, K. Saleh, L. Larger, J. M. Dudley, C. R. Menyuk, and Y. K. Chembo, IEEE Photonics J. **5**, 6100409 (2013).

[12] Z. Qi, G. D'Aguanno, and C. R. Menyuk, J. Opt. Soc. Am. B **34**, 785 (2017).

[13] M. C. Cross and P. C. Hohenberg, Rev. Mod. Phys. **65**, 851 (1993).

[14] P. Franco, F. Fontana, I. Cristiani, M. Midrio, and M. Romagnoli, Opt. Lett. **20**, 2009 (1995).

[15] T. J. Kippenberg, R. Holzwarth, and S. A. Diddams, Science **332**, 555 (2011).

[16] D. Gomila, A. J. Scroggie, and W. J. Firth, Phys. D **227**, 70 (2007).

[17] P. Parra-Rivas, D. Gomila, L. Gelens, and E. Knobloch, Phys. Rev. E **97**, 042204 (2018).

[18] M. Karpov, M. H. P. Pfeiffer, H. Guo, W. Weng, J. Liu, and T. J. Kippenberg, Nat. Phys. **15**, 1071 (2019).

[19] L. A. Lugiato and R. Lefever, Phys. Rev. Lett. **58**, 2209 (1987).

[20] N. Périnet, N. Verschueren, and S. Coulibaly, Eur. Phys. J. D **71**, 401 (2017).

[21] E. Doedel, H. B. Keller, and J. P. Kernevez, Int. J. Bifurcation Chaos Appl. Sci. Eng. **01**, 493 (1991).

[22] S. Wang, A. Docherty, B. S. Marks, and C. R. Menyuk, J. Opt. Soc. Am. B **31**, 2914 (2014).

[23] F. Leo, S. Coen, P. Kockaert, S.-P. Gorza, P. Emplit, and M. Haelterman, Nat. Photon. **4**, 471 (2010).

[24] F. Leo, L. Gelens, P. Emplit, M. Haelterman, and S. Coen, Opt. Express **21**, 9180 (2013).

[25] D. J. Kaup and A. C. Newell, Phys. Rev. B **18**, 5162 (1978).

[26] K. Nozaki and N. Bekki, Phys. D **21**, 381 (1986).

[27] J. Pfeifle, A. Coillet, R. Henriet, K. Saleh, P. Schindler, C. Weimann, W. Freude, I. V. Balakireva, L. Larger, C. Koos *et al.*, Phys. Rev. Lett. **114**, 093902 (2015).

[28] D. C. Cole, E. S. Lamb, P. Del'Haye, S. A. Diddams, and S. B. Papp, Nat. Photonics **11**, 671 (2017).

[29] S. Coen and M. Erkintalo, Opt. Lett. **38**, 1790 (2013).

[30] P. Parra-Rivas, D. Gomila, M. A. Matías, S. Coen, and L. Gelens, Phys. Rev. A **89**, 043813 (2014).

[31] C. Godey, I. V. Balakireva, A. Coillet, and Y. K. Chembo, Phys. Rev. A **89**, 063814 (2014).

[32] D. T. Spencer, T. Drake, T. C. Briles, J. Stone, L. C. Sinclair, C. Fredrick, Q. Li, D. Westly, B. R. Ilic, A. Bluestone *et al.*, Nature (London) **557**, 81 (2018).

[33] C. Kittel, *Introduction to Solid State Physics* (John Wiley & Sons, New York, 2007).

[34] P. Gaspard, *Chaos Scattering and Statistical Mechanics*, Nonlinear Science Series (Cambridge University Press, 1998).